COMPARISON BETWEEN GREEN AND INFRARED LASER IN LASER POWDER BED FUSION OF PURE COPPER THROUGH HIGH FIDELITY NUMERICAL MODELLING AT MESO-SCALE

W.E. ALPHONSO[1]*, M. BAYAT[1] and J.H. HATTEL[1]

[*]*Corresponding author*

[1]*Technical University of Denmark (DTU), 2800, Kgs, Lyngby, Denmark*

ABSTRACT

Laser Powder Bed Fusion (L-PBF) is a Metal Additive Manufacturing (MAM) technology which offers several advantages to industries such as part design freedom, consolidation of assemblies, part customization and low tooling cost over conventional manufacturing processes. Electric coils and thermal management devices are generally manufactured from pure copper due to its high electrical and thermal conductivity properties. Therefore, if L-PBF of pure copper is feasible, geometrically optimized heat sinks and free-form electromagnetic coils can be manufactured. However, producing dense pure copper parts by L-PBF is difficult due to low optical absorptivity to infrared radiation and high thermal conductivity. To produce dense copper parts in a conventional L-PBF system either the power of the infrared laser must be increased above 500W, or a green laser should be used for which copper has a high optical absorptivity. Increasing the infrared laser power can damage the optical components of the laser systems due to back reflections and create instabilities in the process due to thermal-optical phenomenon of the lenses. In this work, a multi-physics meso-scale numerical model based on Finite Volume Method (FVM) is developed in Flow-3D to investigate the physical phenomena interaction which governs the melt pool dynamics and ultimately the part quality. A green laser heat source and an infrared laser heat source are used individually to create single track deposition on pure copper powder bed above a substrate. The effect of the dissimilar optical absorptivity property of laser heat sources on the melt pool dynamics is explored. To validate the numerical model, experiments were conducted wherein single tracks are deposited on a copper powder bed and the simulated melt pool shape and size are compared. As the green laser has a high optical absorptivity, a conduction and keyhole mode melting is possible while for the infrared laser only keyhole mode melting is possible due to low absorptivity. The variation in melting modes with respect to the laser wavelength has an outcome on thermal gradient and cooling rates which ultimately affect the mechanical, electrical, and thermal properties.

Keywords: Pure Copper, Laser Powder Bed Fusion, Finite Volume Method, multi-physics

INTRODUCTION

MAM technologies provides advantages such as low part weight, high design freedom, part customization and low volume production hence it has gained a lot of attention in the last decade from the aerospace, medical and automotive industries [1]. L-PBF is one of the seven Additive Manufacturing technologies where the working principle is based on spreading a

micron-size metal powder on a build plate and using a laser as a heating source to consolidate the powder layer at selected locations according to the sliced CAD geometry. After melting the powder bed, the build plate is lowered by a specific distance and the next layer of powder is coated and melted by the laser. This powder coating and selectively melting steps are repeated in a layer-by-layer fashion which finally leads to a 3D part metal part produced at the end of the process [2]. L-PBF technology also has its disadvantages such as build orientation dependent anisotropy, difficulty in removal of support structures [3] and part defects such as pores, un-melted zones, delamination, warping and residual stresses [4].

L-PBF also many process variables [5] that can affect the final part quality to various degrees and must be optimized to produce a defect-free part, which makes finding the optimal process parameter window for a new material or alloy expensive and time-consuming using a trial-and-error experimental approach. To reduce the experimental cost and increase efficiency of developing a process window for a new material, a fundamental understanding of the thermal-fluid flow phenomena in the melt pool is important. The melt pool is an elementary unit of a 3D printed component, hence any defects formation mechanisms at this scale should be explored. To understand the thermal flow phenomena inside the melt pool experimental in-situ methods such as X-ray imaging, Dynamic X-ray tomography, Schlieren imaging, Optical imaging, Ultrasonic testing, Acoustic Emission Spectroscopy, Optical Emission Spectroscopy, Optical Tomography, Optical Coherence Tomography, Pyrometry and Infrared Imaging are available [6]. However, technologies like X-ray imaging can only be used for single laser track deposition due to their working principle and cannot be implemented in an industrial L-PBF machine. Most of the methods need to be calibrated as they detect a defect signature and not do not observe the actual defect. Hence, physics-based melt pool scale L-PBF numerical methods have been developed to simulate the process so that defect forming mechanisms at different regions of the process window could be identified and new process parameters can be acquired faster for new materials at a relatively low cost. In the meso-scale model, along with the temperature and flow fields, defects such as lack of fusion voids with un-melted powder and gas pores can also be captured [7], [8].

Pure copper produced by L-PBF, however, is a challenge due to copper's intrinsic thermo-electrical properties which make the material appealing for thermal and electrical applications. High thermal conductivity which is desired in cooling devices hinder the L-PBF processing as the deposited thermal energy from the laser is rapidly conducted away from the melt pool and hence less heat is accumulated to melt the material [9]. In addition, the low optical absorptivity of pure copper to infrared laser (1060 nm – 1080 nm) which is commonly used in state-of-the-art L-PBF machines [10] creates an issue as a low effective laser energy is deposited in the powder bed leading to un-melted zones and unstable melt pools. To overcome this challenge, the laser power of the infrared laser in these machines is increased above the standard 400 W. However, by utilizing a high laser power, the reflected radiation can damage the optics in the laser guiding optical system of the L-PBF machine affecting the lifetime of optical components [9]. To tackle these issues green laser source (515 nm) is used in a new generation of L-PBF as copper and other metals like silver, titanium and steel have a higher optical absorptivity at this wavelength [11].

In this work a numerical meso-scale model of the L-PBF process is developed for pure copper where green and infrared heat sources are used individually to consolidate a single

track on a powder bed. To validate the numerical model, experiments under similar conditions were conducted where the solidified melt pools shape and size are used as validation metrics. After validation, the process parameters for the green laser simulation case are altered to change the melting mode from conduction to keyhole thus showcasing the robustness of the model in a different processing mode. Finally, the single-track green laser model is extended to a multiple layer single track model and the numerical results are compared to experiments for validation.

NUMERICAL MODEL

In this work, an FVM framework is used to develop a Computational Fluid Dynamics (CFD) based high fidelity model which includes physics such as thermal and mass transfer, melting and solidification, evaporation, thermal capillarity, surface tension and ray tracing multiple reflections. A Discrete Element Method (DEM) model is used to generate a powder bed consisting of individual discrete spherical shaped powders whose Particle Size Distribution (PSD) is obtained from the experiments. To reduce the complexity of the model further and increase the computational efficiency some assumptions were made and are listed below:

- The fluid in the melt pool is a Newtonian incompressible fluid.
- The flow in the melt pool is laminar and viscous.
- No gas phase is present above the powder bed and this region is treated as void where no temperature, velocity and pressure field calculated.
- The solidification model is linear, and the temperature interval between the solidus and liquidus temperature is 2° K.
- A Gaussian heat source with multiple reflection ray-tracing algorithm is implemented.
- The powder particles are perfectly spherical.
- Powder spattering is not captured during the melting process.
- The phase change from liquid to vapor is solved explicitly affecting the flow and temperature fields.

Deviation from the set process parameters such as thermal lensing phenomenon [12] in the optical system, the gas crossflow over the powder bed and interaction of the vaporized by-products with the incident laser is not captured by the model and these effects can be captured by using other sub-models. The multiple physics involved in single track L-PBF processing of is shown in **Fig. 1**.

FLUID FLOW AND HEAT TRANSFER

The numerical model solves for the temperature and velocity field of the molten metal-induced by the laser heat deposited in the powder layer and substrate. For the fluid flow the Navier Stokes equations of continuity and momentum are solved to obtain the velocity and pressure fields during the laser melting process as shown in Eq. (1) and Eq. (2) respectively [8]

$$\vec{\nabla}\cdot(\vec{V})=0 \tag{1}$$

$$\rho\left[\frac{\partial}{\partial t}(\vec{V})+\vec{V}\cdot\vec{\nabla}(\vec{V})\right] = -\vec{\nabla}p+\vec{\nabla}\cdot\left[\mu\left(\vec{\nabla}\vec{V}+\vec{\nabla}\vec{V}^{T}-\frac{2}{3}\vec{\nabla}\cdot\vec{V}\right)\right] - \frac{K_c(1-f_l)^2}{C_k+f_l^3}\vec{V}-\rho\vec{g}\beta(T-T_i) \tag{2}$$

Here V (m/s) is the velocity vector and p (Pa) is pressure. The second term on the right-hand side of Eq. (2) represents the forces caused by viscous stresses and the third term is the solidification drag force due to the formation of a mushy zone. K_C (kg/m^{3}s) and C_k (-) are the constants used for solidification drag forces and they are typically in the order of 10^6 and 10^{-4}, respectively. The last term in Eq. (2) accounts for the buoyancy effect. In this work the flow is assumed to be incompressible and hence to model the buoyancy force, the Boussinesq approximation has been used where β (1/K) is the thermal expansion coefficient. The fluid flow is coupled with the heat transfer using the energy equation as shown in Eq. (3)

$$\rho\left[\frac{\partial}{\partial t}(h)+\vec{V}\cdot\vec{\nabla}(h)\right]=\vec{\nabla}\cdot\left[k_{bulk}(\vec{\nabla}T)\right] \tag{3}$$

$$h=h_{ref}+C_{p,\,bulk}(T-T_{ref})+f_l\Delta H_{sl} \tag{4}$$

$$f_l = \begin{cases} 0 & T < T_s \\ \dfrac{T-T_s}{T_l-T_s} & T_s \le T \le T \\ 1 & T > T_l \end{cases} \tag{5}$$

Where h (kJ/kg) is the specific enthalpy of the metallic phase, and the subscript 'ref' stands for the reference state from which the enthalpy is evaluated. f_l (-) is the liquid fraction function defined in Eq. (5), which for simplicity is approximated by a linear function of temperature in the solidification interval and ΔH_{sl} (kJ/kg) in Eq. (4) is the latent heat of fusion. Here the liquid fraction varies linearly between the solidus and liquidus temperatures.

For the material properties such as density, thermal conductivity and specific heat capacity in the solidification interval, the values are calculated by using the liquid f_l (-) and solid fractions f_s (-) as shown in Eq. (6), (7) and (8).

$$\rho=f_s\rho_s+f_l\rho_l \tag{6}$$

$$k_{bulk}=f_sk_s+f_lk_l \tag{7}$$

$$C_{p,\,bulk}=\frac{f_s\rho_sC_{p,s}+f_l\rho_lC_{p,l}}{f_s\rho_s+f_l\rho_l} \tag{8}$$

Where the subscript 's' refers to solid and '*l*' refers to liquid.

To track the interface between the void and the metal phases, a Volume of Fluid (VOF) method is used. The free surface is captured using Eq. (9) where the value of the scalar *F* (-) varies between zero to one.

$$\frac{\partial}{\partial t}(F)+\vec{\nabla}\cdot(F\vec{V})=0 \tag{9}$$

Intermediate values of *F* indicate an interface between these two immiscible phases. In this work, the calculation for the gas phase is not included because an assumption is made that the gas flow has an insignificant impact on the melt flow characteristics. Hence, the gas phase is treated as a void with no fluid and thermal properties are assigned to these cells.7

INTERFACIAL FORCES

One of the driving forces in the melt pool is the thermo-capillary effect also known as Marangoni effect which occurs due to the variation in surface tension of the molten metal with temperature. To account for this phenomenon in the model, a shear stress is defined on the free surface of the melt pool, which causes the molten pool to widen with increasing temperature in the case of a negative surface tension gradient and deepen when the gradient is positive [13]. The change of surface tension with temperature for pure copper is shown in **Table 1** and is a linear function. Here the surface tension gradient is active between the liquidus and evaporation temperature, where the metal is in a complete fluid state.

In L-PBF, a micron size laser heat source is used to melt the powder and hence very high temperatures near the boiling point can be achieved leading to localized vaporization where the metal changes its phase from liquid to vapor. This metal vapor phase in turn generates a pressure on the surface of the melt pool, creating a depression zone. This pressure is denoted as recoil pressure and is accounted for in the model as a pressure acting perpendicular to the free surface without implicitly modelling the liquid to vapor phase transition. In summary, the recoil pressure, Marangoni shear force, and surface tension are all acting on the free surface and the force balance at the metal-void interface is expressed by Eq. (10).

$$F_{V/F} = [P_{recoil}+\sigma.\kappa]\vec{n} + [\vec{\nabla}T-\vec{n}(\vec{\nabla}T.\vec{n})]\frac{d\sigma}{dT} \tag{10}$$

The second term on the right-hand side of Eq. (10) is the Marangoni shear stress and $d\sigma/dT$ ($kg.s^2.K^{-1}$) represents the dependency of surface tension on temperature and acts tangential to the free surface of the fluid. P_{recoil} (Pa) is the pressure acting normal to the free surface of the melt pool when temperatures are near the boiling point of the metal and κ (m^{-1}) is the curvature of the free surface of the fluid, whereas '*n*' denotes the normal direction to the interface.

The recoil pressure in the first term Eq. (10) can be expanded and is shown in Eq. (11).

$$P_{recoil}(T) = 0.54P_{atm}\, e^{\left[\frac{\Delta H_{lv}}{C_v(\gamma-1)}\left(\frac{1}{T_g}-\frac{1}{T}\right)\right]} \tag{11}$$

Where, P_{atm} (Pa) is atmospheric ambient pressure, γ is the specific heat ratio, ΔH_{lv} (kJ/kg) is the latent heat of vaporization and T_g is the vaporization temperature.

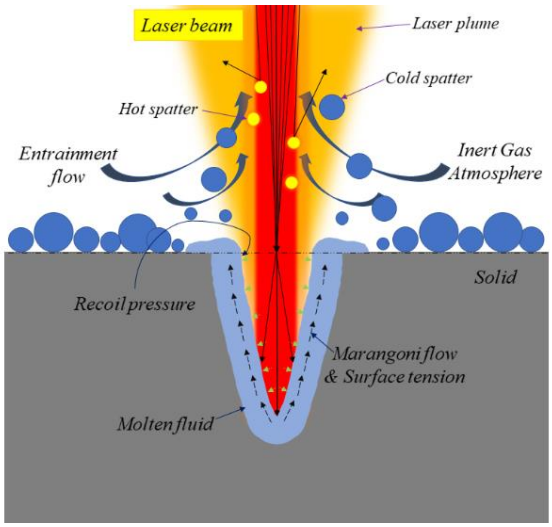

Fig. 1 Multi-physics phenomena in the laser-material interaction zone

RAY TRACING HEAT SOURCE

The heat source in the model is a laser spot with a predefined diameter that traverses along the powder bed with a particular scanning speed. This laser spot generates an input heat flux into the computational domain and has a Gaussian distribution around the center axis of the laser beam according to Eq. (12).

$$q''_{laser}(x,y) = \frac{2P}{\pi R^2} e^{\left(-\frac{2\left((x-x_{laser})^2+(y-y_{laser})^2\right)}{R^2} \right)} \tag{12}$$

Where P (J/s), R (m), x_{laser} (m) and y_{laser} (m) are laser power, laser beam spot radius, x coordinate and y coordinate of the initial laser position. When the laser is traversing in a straight line in the x-direction, y is equal to 0 and x is equal to $v \cdot t$, where v is laser scanning speed and t is time. The laser heat flux is discretized from a continuous Gaussian distribution according to the mesh size. The size of the cell determines the discretization of the laser heat flux as well as the number of rays being generated. The incident rays from the laser undergoes multiple reflections on the melt pool surface and upon every interaction of the ray with the molten metal, the energy of the reflected ray is reduced by a certain amount depending on the optical absorptance value. More details on the ray-tracing algorithm applied in L-PBF can be found in the previous works by the author group [8].

DOMAIN AND BOUNDARY CONDITIONS

The discrete powder layer for the CFD numerical model is obtained by implementing the DEM where each powder particle is modelled as a sphere and the powder motion is governed by Newton's second law. The DEM modelling is based on a Lagrangian framework where the Hertz-Mindlin contact model is used to capture the collision between particles. In this work, a deposition method is usually denoted as the 'rain-drop' method is used wherein powder particles are dropped from the top of the domain on the bulk/substrate region [14]. The bottom and the side face of the domain are treated as walls and the particles are hence trapped inside the numerical domain. The 'rain-drop' is extremely computationally efficient, as compared to modelling the actual powder deposition process in a L-PBF system where a roller or a spreader is used to deposit thin powder layers. The DEM simulation is halted as soon as the pre-determined powder layer thickness is obtained, and later the powder particles deposited are exported to the CFD model. The particle size distribution (PSD) of the powder used in the DEM model is obtained from size measurements of the copper powder used in the experiments.

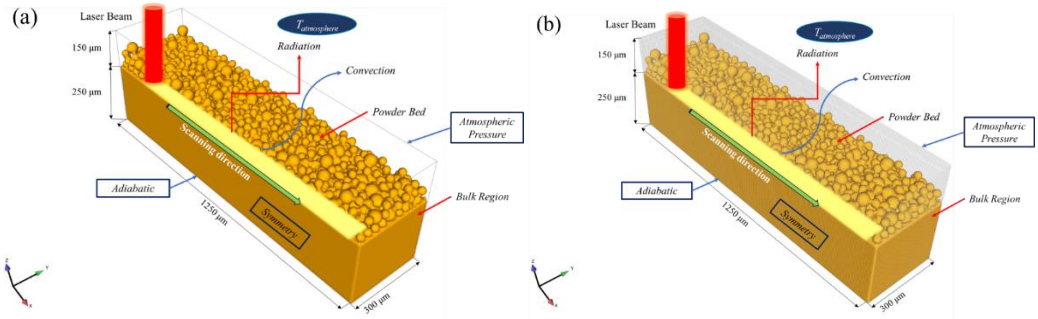

Fig. 2 Framework for single laser track simulation model including powder bed and substrate (a) computational domain with boundaries (b) discretization of the domain with uniform quad mesh.

The size of the numerical domain is 1250 µm x 600 µm x 400 µm for the single-track models. The substrate/bulk region is 250 µm thick and a powder layer thickness of 100 µm is deposited over it as shown in **Fig. 2**(a). The prescribed laser scanning direction is also shown to be along the x-direction. To reduce computation time, the numerical domain is halved at the laser beam center along the x-z plane and a symmetry boundary condition is applied. The substrate thickness was increased in simulation cases where the melt pool interacts with the bottom of the domain. The material assigned to the powder bed and substrate is pure copper and the thermo-physical properties used in this work is shown in **Table 1**. An adiabatic condition is applied at bottom and the side walls of the domain while the top surface is assigned as a pressure outlet. The thermal boundary condition applied on the exposed top surface of the melt pool and is expressed by Eq. (13) and is also shown in **Fig. 2**.

$$-k\frac{\partial T}{\partial \vec{n}} = \varepsilon\sigma_{rad}\left(T_{amb}^4 - T^4\right) + h_{amb}\left(T_{amb} - T\right) - q''_{laser} + q_{vap} \tag{13}$$

where, ε (-) and σ_{rad} (W/m^2/K^4) represent the emissivity and Stephan-Boltzmann constants respectively, h_{amb} (W/m^2/K) represents convective heat transfer coefficient, q''_{laser} (W.m^{-2}) is the laser heat flux and q_{vap} is the heat loss due to vaporization. The region which is 150 µm in height from the top surface of the bulk region is assigned as a void, so the movement of the free surface interface can be tracked. **Fig. 2**(b) shows the discretized computational domain with cubic mesh cells which are 5 µm in size. The cell size is selected based on a mesh independency study, wherein an optimized mesh size is obtained that is a compromise between numerical accuracy and computational efficiency.

Table 1 Thermo-physical properties of pure copper

Parameter	Symbol	Value	Units
Density at Room temperature	ρ	8920	kg/m^3
Viscosity	μ	0.41	kg/m/s
Liquidus Temperature	T_l	1357	K
Solidus Temperature	T_s	1355	K
Boiling Temperature	T_b	3220	K
Latent heat of Fusion	ΔH_{sl}	$0.206 \cdot 10^6$	J/kg
Latent heat of Evaporation	ΔH_{lv}	$4.69 \cdot 10^6$	J/kg
Ambient Convective heat transfer	h_{amb}	80	W/m^{2}K
Surface tension gradient	γ	-0.000286	kg/s^2/K
Surface tension at liquidus temperature	σ	0.1304	kg/s^2
Surface emissivity	ε	0.1	-

It should be noted that pure copper has no solidification interval but to capture the release of latent heat during the melting process, a 2 °K solidification interval is added in the model. It is assumed that the numerical result will be insignificantly affected by using such a narrow solidification interval.

RESULTS AND DISCUSSION

GREEN LASER SINGLE TRACK DEPOSITION

For the green laser heat source numerical model two sets of process parameters are selected for validating the numerical accuracy. The first set of process parameters creates a conduction mode melting during laser scanning due to a low Volumetric Energy Density (VED). VED (J/m^3) can be defined by the Eq. (14) [15].

$$VED = \frac{P}{v.d.t} \tag{14}$$

where P is the laser power (W), v is the scanning speed (mm/s), d is the laser beam spot size (µm) and t is the powder layer thickness (µm). VED condenses all the important process parameters into a single parameter. The second parameter set has a high VED value which

causes a keyhole mode melting. The process parameters used in these two cases is shown in **Table 2**.

Table 2 Process parameter for single track green L-PBF numerical model

Process Parameter	Low Energy Density	High Energy Density
Power (W)	485	768
Scanning Speed (mms^{-1})	500	500
Beam size (μm)	150	150
Powder layer thickness (μm)	100	100
VED (J/mm^3)	65	103

After solving the numerical model, a 2D melt pool contour is extracted at a location along the laser scanning direction where the melt pool has attained a pseudo-steady state i.e., the melt pool size and shape do not vary. The location where the melt pool contour is extracted in each case depends on the value of VED and with a high VED this location is shifted further away from the laser's initial position as it takes longer for the thermo-fluid conditions in the melt pool to stabilize and reach a pseudo-steady state. Therefore, for the high VED case, the melt pool is validated at two locations, 3mm and 7mm away from the start of the single track. The experimental results are taken from the work of [16] where a similar green laser system is utilized when compared to the laser system used to manufacture the single-track thin wall structure investigated in future sections. The PSD of the pure copper powder used for the DEM modelling for the green laser numerical model was also taken from the same work to maintain consistency. The 2D melt pools from the simulation model and experiments are qualitatively compared in **Fig. 3** where the model predicts accurately the melt pool shape and size for both melting modes. The measured melt pool dimensions are shown in **Table 3** along with the calculated error % which is the difference between the simulation and experimental result. In the numerical result, the melted and non-melted regions is defined as the regions of the metal phase that underwent phase transition from solid to liquid during the laser melting process.

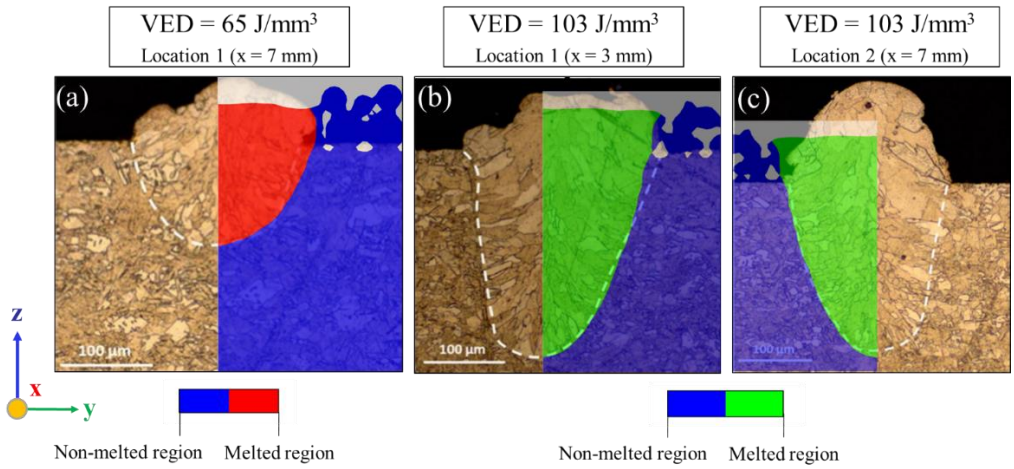

Fig. 3 2D melt pool contours from the numerical model compared to experiments [16] for (a) VED = 65 J/mm^3 at 7 mm from the beginning of the single track (b) VED = 103 J/mm^3 at 3 mm from the beginning of the single track (c) VED = 103 J/mm^3 at 7 mm from the beginning of the single track. In the 2D contour, the non-melted region is indicated in blue, and the melted region is indicated by red and green when the VED is 65 J/mm^3 and 103 J/mm^3 respectively.

Table 3 Comparison of melt pool sizes from experimental and numerical results for single track green L-PBF process

Source	Location	VED (J/mm^3)	Melt pool width (µm)	Error in width (%)	Melt Pool depth (µm)	Error in depth (%)
Experiment	1	65	183		107	
Simulation			200	-9	102	5
Experiment	1	103	238		245	
Simulation			256	-8	237	3
Experiment	2		214		222	
Simulation			256	-20	237	-7

The simulated melt pool matches very well with the experiments and this because the numerical model accounts for all three major physical phenomena occurring in the melt pool during the L-PBF process as explained earlier. The error in the melt pool depth and width can be accounted to the assumptions and simplifications made in the model to successfully compute the melting and solidification process of the powder bed. Melt pool height was not used as a metric to validate the numerical model due to powder spattering and entrainment phenomenon omitted in the model. The 3D temperature contour at time = 1.8 µs for the two process parameters selected is shown in **Fig. 4** along with the location where the pseudo-steady 2D melt pool contours were extracted for validation. It should firstly be noted that both selected process parameters can consolidate the powder layer successfully without any defect

formation such as un-melted zones and gas pores. A VED of 65 J/mm^3 creates a shallow U-shaped melt pool with a small melt volume due to less heat energy from laser as shown in **Fig. 4**(a). At the low VED setting, heat is rapidly dissipated away from the melt pool and hence the dominant heat transfer mechanism is conduction due to the intrinsic high thermal conductivity of copper. A VED of 103 J/mm^3 creates a deep and wide melt pool as shown in **Fig. 4**(b) due to the combining effect of high optical absorptivity to green laser radiation and multiple reflection in the deep vapor depression. The keyhole shaped vapor depression is created due to the rise in local temperature above the boiling point and due to this geometry, multiple laser rays are trapped inside the keyhole due to the multiple reflection (Fresnel absorption) phenomenon, thereby increasing the absolute absorptivity. Hence, a larger melt pool is created and the energy coupling efficiency between the laser and the powder bed is increased. The width of the partially melted powder zone on the edges of the melt pool is small and has constant width when the VED is 65 J/mm^3 when compared to when the VED is 103 J/mm^3 thus indicating better stability in the conduction melting mode. Hence, green laser process parameters with VED ~ 65 J/mm^3 should be implemented in melting the contours to reduce surface roughness and increase the dimensional tolerance of the part. The process parameters with VED ~ 103 J/mm^3 can be implemented in the bulk regions where larger melting zones for each laser scan track is desired to increase the productivity without forming pore defects.

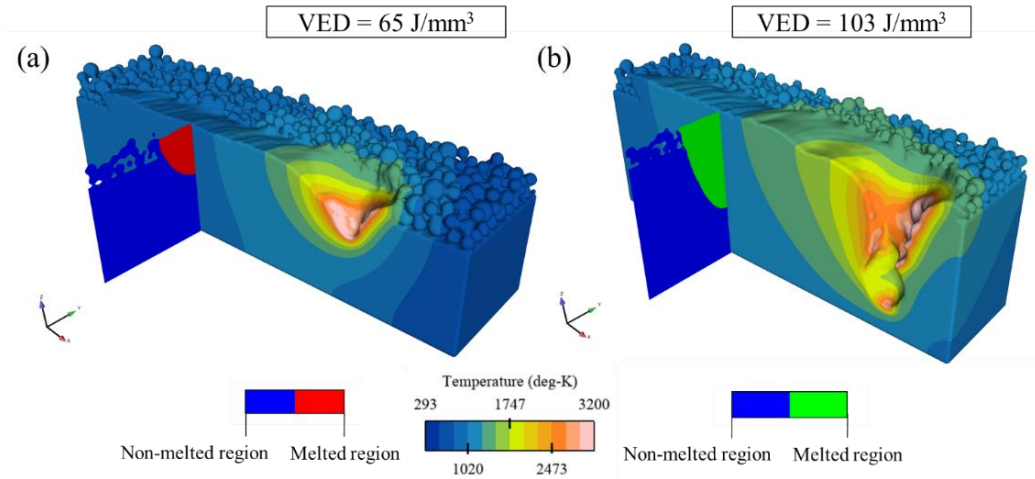

Fig. 4 3D temperature contour plots of during single track L-PBF process at time1.8 μs when (a) VED = 65 J/mm3 (b) VED = 103 J/mm3 along with 2D melt pool contours at 5 mm from the laser initial position. In the 2D contour, the non-melted region is indicated in blue, and the melted region is indicated by red and green when the VED is 65 J/mm^3 and 103 J/mm^3 respectively.

The optical absorptivity for the green laser is 40% and is implemented as an input parameter in the green laser heat source model [17], [18].

INFRARED LASER SINGLE TRACK DEPOSITION

Like the green laser model, an infrared laser model is developed for a single-track L-PBF process. However, due to the low optical absorptivity of copper to infrared radiation, the process parameter window for successful melting of the powder bed is narrow. It is difficult to obtain conduction dominant U-shaped melt pools by using an infrared laser unlike the green laser heat source showed in **Fig. 3**(a). Therefore, a single parameter set which produces keyhole melting mode was selected for validation and the parameter values are shown in **Table 4**.

Table 4 Process parameter for single track infrared L-PBF meso-scale numerical model

Process Parameter	Values
Power (W)	540
Scanning Speed (mm/s)	500
Beam size (μm)	45
Powder layer thickness (μm)	100

The calculated VED for the selected process parameters is 240 J/mm^3, which is more than twice the value of the energy density implemented in the green laser simulation model. This is due to a selection of a smaller laser beam spot size which is a third used in the green laser model. For validating the model, an experimental result from the work of [19] was chosen where an infrared laser was used for consolidating the powder bed. Like the green laser model, a 2D melt pool contour is taken at a location along the laser scanning direction where the melt pool attains a pseudo-steady state. For the simulation case, a mesh size of 5 μm was used as the size of the computational domain and the powder layer thickness were similar to the single track green laser model. The 2D melt pools contour from the simulation model is compared to the experimental results and is shown in **Fig. 5**(a). The numerical model predicts the melt pool shape accurately for the selected process parameter. The melt pool dimensions of the simulated and experimental results are shown in **Table 5** along with the calculated error %.

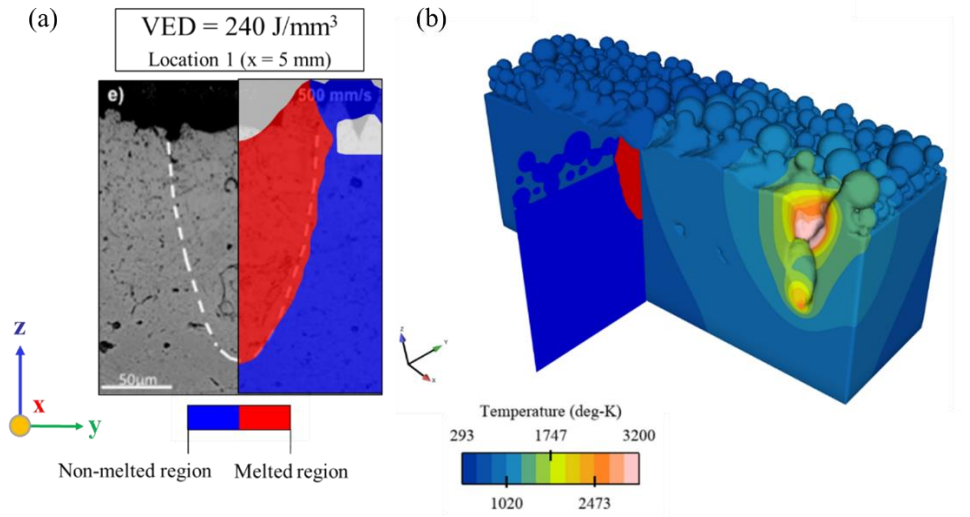

Fig. 5 (a) 2D melt pool contours from the meso-scale numerical model compared to experiments [19] for VED = 240 J/mm^3 at 5 mm from the beginning of the single track. In the 2D contour, the non-melted region is indicated in blue, and the melted region is indicated by red color. (b) 3D temperature contour plot at time1.8 μs when VED = 240 J/mm^3 along with 2D melt pool contour at 5 mm from the laser initial position.

Table 5 Comparison of melt pool dimensions from experimental and numerical results for single track infrared L-PBF process

Source	Melt pool width (μm)	Error in width (%)	Melt Pool depth (μm)	Error in depth (%)
Experiments	103		147	
Simulation	124	-21	147	0.4

The error in the melt pool width is four times the mesh size used and therefore it can be accounted to the assumptions made in the numerical model. Along with the other multi-physics phenomena included in the numerical model, recoil pressure and the multiple reflection heat source accurately deposits thermal energy into the powder bed especially when a high VED is implemented, which is shown by less than 1% error in the melt pool depth. At high laser powers, the vapor depression formed on the surface of the melt pool traps the laser radiation increasing the energy coupling efficiency. For an infrared laser, when the laser power is reduced the local temperature in the melt pool is decreased which leads to smaller and shallower melt pool without a keyhole shaped depression zone. Furthermore, the amount of laser ray trapping in the melt pool is reduced resulting in decrease in the energy coupling efficiency and absolute absorptivity. When the absolute absorptivity is the low, the melting mode is conduction dominated which leads to melt pool instability and increase in un-melted zone. There for infrared laser heat sources, successful consolidation of a powder bed can only

be achieved in keyhole melting mode. For the validated model, the optical absorptivity of the infrared laser is 12% and is implemented as an input parameter in the multiple reflection ray-tracing model.

The 3D temperature contour for the VED values selected for the single-track L-PBF processing is shown in **Fig. 5**(b) along with a 2D melt pool contour when the melt pool attains a pseudo-steady state. When implementing a VED = 240 J/mm^3, a keyhole melting mode is obtained and due to the multiple reflection effect, the energy coupling is increased thus leading to an increase in the melt pool depth and ultimately melt pool volume. The low optical absorptivity of 12% increases the dependence of the energy coupling efficiency solely on the multiple reflection phenomenon which becomes significant at high laser powers due to formation of a keyhole. Processing at such high VED leads to the formation of keyhole induced porosity seen in **Fig. 5**(b) in the solidified region due to instability in the depression zone. Comparing the melt pool depth of an infrared heat source with a VED = 240 J/mm^3 and a green heat source with a VED =103 J/mm^3, it is predicted that the green laser creates a deeper melt pool even with a bigger laser spot size is used.

GREEN LASER THIN WALL DEPOSITION

The validated single track green laser model in the previous section is extended to a multi-layer single track L-PBF model. In this model framework, the CFD and DEM solvers are one-way coupled to form a thin wall structure. The framework is similar to the work done in previous work done by the author's group and is explained in [8]. After melting a single track using the CFD solver, the powder bed is allowed to cool to room temperature (300°K). Later the consolidated powder bed is exported in CAD format from the CFD solver to the DEM model and is assigned as a solid region. In the DEM solver, a powder layer is deposited by the 'rainfall method' over the solidified single track and the remaining un-melted powder regions. The new powder layer along with the solidified single track is imported into the CFD model and a single track is consolidated on the new powder layer. Therefore, in such a way ten single tracks are consolidated one above other along with the un-melted powders powder bed.

To validate the model, a thin wall feature which is made from multiple layers of single-track deposition is printed using a Truprint 1000 green edition L-PBF system. The thin wall feature is scanned using an industrial ZEISS XRadia 520 Versa X-ray CT instrument which was operated at 160 kV with a HE6 filter and a 4X objective. After scanning the thin-wall feature, the generated 1601 2D tomograms were filtered using appropriate de-nosing algorithms and later reconstructed into a 3D volume which was used for conducting thickness measurements. The process parameters used the print the thin wall on the L-PBF machine is shown in **Table 6**. The PSD used in the DEM model was obtained from the pure copper powder measurement done using Malvern Panalytical Mastersizer 3000 which is based on laser diffraction principle.

Table 6 Process parameters used to print thin wall structure

Process Parameters	Values
VED	135 J/mm^3
Laser type	Continuous wave
Powder layer thickness	30 µm
Laser beam spot size	200 µm

Instead of scanning the entire thin wall feature, a small portion of the wall is scanned at a higher resolution with a voxel size of 3 µm and exposure time of 18 s. The spatial resolution is higher when compared to scan of the entire thin wall which generated a voxel size of 9 µm and an exposure time of 4 s was used. With a larger voxel size intricate features such as the micron size copper powders sintered to the side surfaces cannot be accurately resolved. The wall thickness measured from the X ray-CT is compared with the numerical thickness calculated from the 2D temperature contours. Temperatures above 1025°K [20] are assumed to cause powder sintering to the sidewalls after a single laser track is scanned on the powder bed. The numerical thickness is measured after each layer deposition and therefore ten wall thicknesses are measured and the measured location after each layer deposition is shown in **Fig. 6**. A 2D plane perpendicular to the laser travel direction is located at the center of the laser beam axis during each layer deposition where the temperature field during each layer deposition. The wall thickness is measured after each layer deposition and the thickness is determined based on the width of the temperature iso-line 1025°K which is the sintering temperature of copper powder.

10 thickness measurements along the build direction were obtained from the X-ray CT data and the distance between the measurement location is equidistant as shown in **Fig. 7**. The thickness measurements from the numerical model and the experiments are shown in **Table 7** along with the calculated error %.

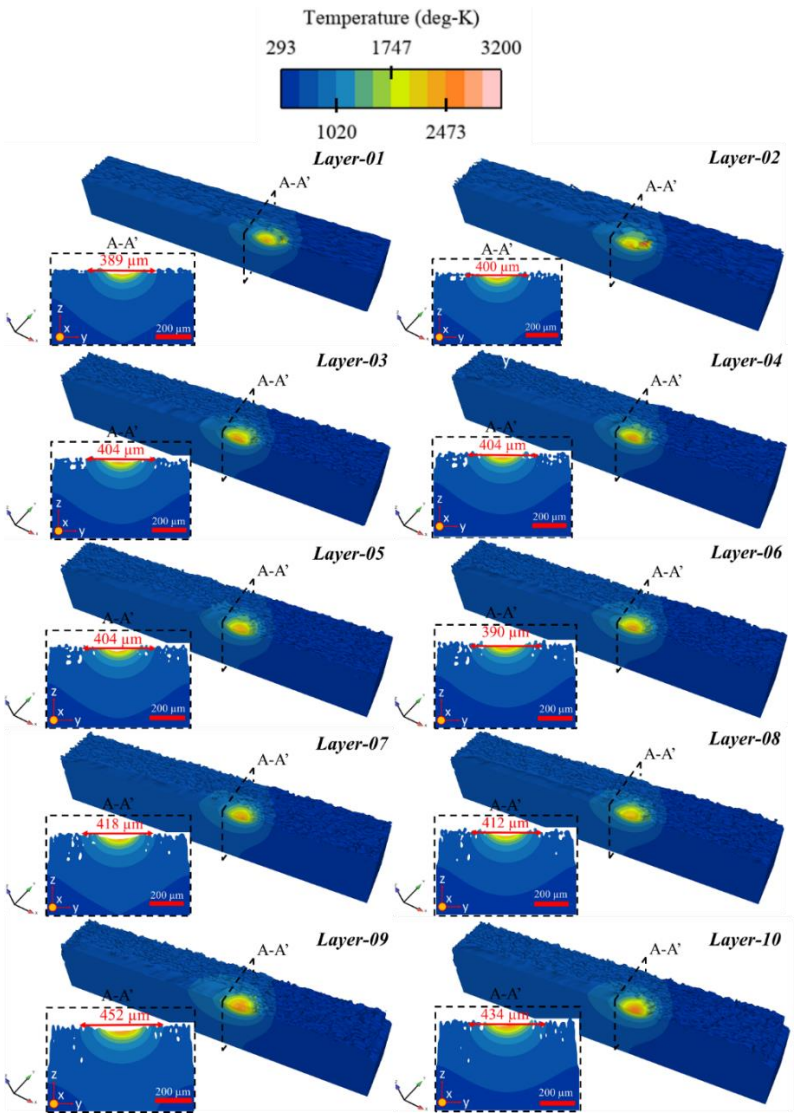

Fig. 6 3D temperature contour during the deposition of a single track in each layer at t = 3 µs. An inset image with each layer deposition depicts a 2D temperature contour on a plane located at the center of the laser and the width of heat affected zone is measured.

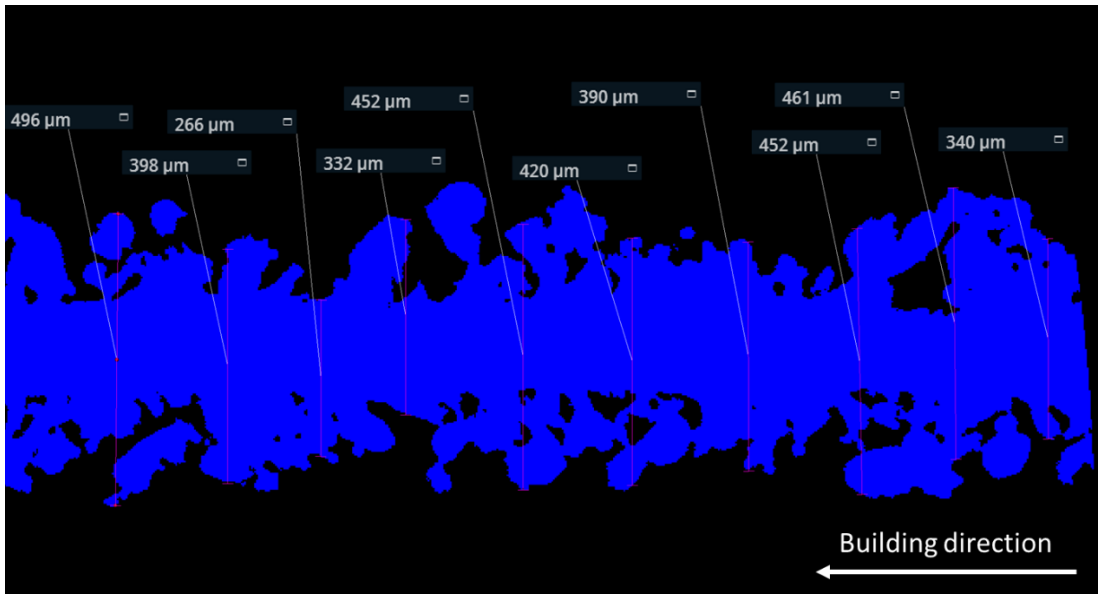

Fig. 7 Wall thickness measured at a 2D cross-section obtained from X-ray CT at 10 locations equidistant from each other.

Table 7 Comparison of wall thickness from experimental and numerical results for single track multi-layer green L-PBF process.

Location	Numerical thickness (µm)	Experimental thickness (µm)	Error %
1	389	340	-14
2	400	461	13
3	404	452	11
4	404	390	-4
5	404	420	4
6	390	452	14
7	418	332	-26
8	412	226	-82
9	452	398	-13
10	434	496	12
Average	411 ± 19	397 ± 76	-4

From **Table 7**, the error % in the predicted wall thickness from the numerical meso-scale model has an average value of 4% which is accurate and acceptable. However, at some locations the error % is quite high and this is due to the randomly packed powder bed used in the numerical model. Therefore, it is shown that the meso-scale numerical model can be used

to predict the actual thickness of thin-wall structures consisting of single-layer depositions accurately.

CONCLUSION

In this work a high fidelity meso-scale L-PBF model is developed for pure copper based on FVM method in Flow-3D. Green and infrared laser hear sources were used individually to consolidate the pure copper powder bed deposited over a substrate. The single-track simulation model was validated by comparing the numerical results with experiments where the melt pool shape and size were the quality metrics. The green laser heat source could generate a larger melt pool as compared to the infrared heat source at a lower VED as the absorptivity is higher in the former. In addition, a thin wall structure consisting of single tracks deposited over each other was simulated using a coupled DEM-CFD model and the results were compared with experiments. Wall thickness was used as a quality metric to validate the multi-layer single track model.

Therefore, a green laser is an efficient heat source for processing pure copper in an L-PBF system wherein both conduction mode and keyhole mode melting are possible while with an industrial standard infrared laser only keyhole melting mode is achievable at high laser powers leading to process instabilities.

APPENDICES AND ACKNOWLEDGEMENTS

This work has received funding from Independent Research Fund Denmark, DIGI-3D project.

References

[1] L. Jyothish Kumar, P. M. Pandey, and D. I. Wimpenny, *3D printing and additive manufacturing technologies*. Springer Singapore, 2018. doi: 10.1007/978-981-13-0305-0.

[2] T. DebRoy *et al.*, "Additive manufacturing of metallic components – Process, structure and properties," *Progress in Materials Science*, vol. 92, pp. 112–224, 2018, doi: 10.1016/j.pmatsci.2017.10.001.

[3] C. S. Lefky, B. Zucker, D. Wright, A. R. Nassar, T. W. Simpson, and O. J. Hildreth, "Dissolvable Supports in Powder Bed Fusion-Printed Stainless Steel," *3D Printing and Additive Manufacturing*, vol. 4, no. 1, pp. 3–11, 2017, doi: 10.1089/3dp.2016.0043.

[4] J. L. Bartlett and X. Li, "An overview of residual stresses in metal powder bed fusion," *Additive Manufacturing*, vol. 27, no. January, pp. 131–149, 2019, doi: 10.1016/j.addma.2019.02.020.

[5] I. H. Ahn, "Determination of a process window with consideration of effective layer thickness in SLM process," *International Journal of Advanced Manufacturing Technology*, vol. 105, no. 10, pp. 4181–4191, 2019, doi: 10.1007/s00170-019-04402-w.

[6] R. McCann *et al.*, “In-situ sensing, process monitoring and machine control in Laser Powder Bed Fusion: A review,” *Additive Manufacturing*, vol. 45, no. May, 2021, doi: 10.1016/j.addma.2021.102058.

[7] M. Bayat *et al.*, “Keyhole-induced porosities in Laser-based Powder Bed Fusion (L-PBF) of Ti6Al4V: High-fidelity modelling and experimental validation,” *Additive Manufacturing*, vol. 30, no. August, p. 100835, 2019, doi: 10.1016/j.addma.2019.100835.

[8] M. Bayat, S. Mohanty, and J. H. Hattel, “Multiphysics modelling of lack-of-fusion voids formation and evolution in IN718 made by multi-track/multi-layer L-PBF,” *International Journal of Heat and Mass Transfer*, vol. 139, pp. 95–114, 2019, doi: 10.1016/j.ijheatmasstransfer.2019.05.003.

[9] S. D. Jadhav, L. R. Goossens, Y. Kinds, B. van Hooreweder, and K. Vanmeensel, “Laser-based powder bed fusion additive manufacturing of pure copper,” *Additive Manufacturing*, vol. 42, no. March, 2021, doi: 10.1016/j.addma.2021.101990.

[10] S. D. Jadhav, S. Dadbakhsh, L. Goossens, J. P. Kruth, J. van Humbeeck, and K. Vanmeensel, “Influence of selective laser melting process parameters on texture evolution in pure copper,” *Journal of Materials Processing Technology*, vol. 270, no. January, pp. 47–58, 2019, doi: 10.1016/j.jmatprotec.2019.02.022.

[11] H. Siva Prasad, F. Brueckner, J. Volpp, and A. F. H. Kaplan, “Laser metal deposition of copper on diverse metals using green laser sources,” *International Journal of Advanced Manufacturing Technology*, vol. 107, no. 3–4, pp. 1559–1568, 2020, doi: 10.1007/s00170-020-05117-z.

[12] L. R. Goossens, Y. Kinds, J. P. Kruth, and B. van Hooreweder, “On the influence of thermal lensing during selective laser melting,” *Solid Freeform Fabrication 2018: Proceedings of the 29th Annual International Solid Freeform Fabrication Symposium - An Additive Manufacturing Conference, SFF 2018*, no. December, pp. 2267–2274, 2020.

[13] M. Bayat, V. K. Nadimpalli, D. B. Pedersen, and J. H. Hattel, “A fundamental investigation of thermo-capillarity in laser powder bed fusion of metals and alloys,” *International Journal of Heat and Mass Transfer*, vol. 166, p. 120766, 2021, doi: 10.1016/j.ijheatmasstransfer.2020.120766.

[14] H. Chen, Q. Wei, Y. Zhang, F. Chen, Y. Shi, and W. Yan, “Powder-spreading mechanisms in powder-bed-based additive manufacturing: Experiments and computational modeling,” *Acta Materialia*, vol. 179, pp. 158–171, 2019, doi: 10.1016/j.actamat.2019.08.030.

[15] S. K. Nayak, S. K. Mishra, C. P. Paul, A. N. Jinoop, and K. S. Bindra, “Effect of energy density on laser powder bed fusion built single tracks and thin wall structures with 100 µm preplaced powder layer thickness,” *Optics and Laser Technology*, vol. 125, May 2020, doi: 10.1016/j.optlastec.2019.106016.

[16] G. Nordet *et al.*, “Absorptivity measurements during laser powder bed fusion of pure copper with a 1 kW cw green laser,” *Optics & Laser Technology*, vol. 147, no. April 2021, p. 107612, 2022, doi: 10.1016/j.optlastec.2021.107612.

[17] M. Hummel, C. Schöler, A. Häusler, A. Gillner, and R. Poprawe, “New approaches on laser micro welding of copper by using a laser beam source with a wavelength of 450 nm,” *Journal of Advanced Joining Processes*, vol. 1, no. February, p. 100012, 2020, doi: 10.1016/j.jajp.2020.100012.

[18] M. Hummel, M. Külkens, C. Schöler, W. Schulz, and A. Gillner, “In situ X-ray tomography investigations on laser welding of copper with 515 and 1030 nm laser beam sources,” *Journal of Manufacturing Processes*, vol. 67, no. April, pp. 170–176, 2021, doi: 10.1016/j.jmapro.2021.04.063.

[19] L. Gargalis *et al.*, “Determining processing behaviour of pure Cu in laser powder bed fusion using direct micro-calorimetry,” *Journal of Materials Processing Technology*, vol. 294, no. March, p. 117130, 2021, doi: 10.1016/j.jmatprotec.2021.117130.

[20] A. Mondal, D. Agrawal, and A. Upadhyaya, “Microwave heating of pure copper powder with varying particle size and porosity,” *Journal of Microwave Power and Electromagnetic Energy*, vol. 43, no. 1, pp. 4315–43110, 2009, doi: 10.1080/08327823.2008.11688599.